Prediction and numerical simulation of droplet impact erosion on metallic structure

G. COUDOUEL[1,2,*], A. COMBESCURE[1], J.-C. MARONGIU[2]

1. LaMCoS, UMR CNRS 5259, Institut National des Sciences Appliquées de Lyon (INSA) - {alain.combescure, guillaume.coudouel}@insa-lyon.fr
2. ANDRITZ Hydro - jean-christophe.marongiu@andritz.com

Abstract

The aim of this work is to understand the erosion mechanism caused by repeated water droplets impingement on a metallic structure, and then perform numerical simulations of the damage. When a high velocity water droplet with small diameter impacts a rigid surface, interaction is driven by inertial effects. Upon impact, the "water-hammer" pressure appears by inertial effect at the center of the contact though the maximum pressure occurs on the envelope of the contact area. Lateral jetting occurs by compression when the wave front travelling inside droplet overtakes the contact area. Concerning the structure, erosion is due to fatigue cracking. First, material grains are weakened during an "incubation" phase. After a large number of impacts, micro-cracks emerge and lead to ejection or fracture of grains, what is called "amplification" phase. A 2-way coupling computation with fluid-structure interaction at macroscopic scale allows to confirm the fatigue-based mechanism by observing the hydrostatic stress. Finally, erosion program developed with two criteria : a general one and Dang Van criterion. It provides the location of the most eroded zones of the structure during a loading cycle. They locate at the edge of jetting zone, which shows the influence of microjets in the erosion mechanism.

Keywords : impact / coupling / droplet / erosion / fatigue

Nomenclature

Scalars

Parameter	Description	Unit (ISO)
c_f	Sound velocity of fluid	$\mathrm{m.s^{-1}}$
c_f^0	Initial sound velocity of fluid	$\mathrm{m.s^{-1}}$
$\hat{c}_f$	Compression waves velocity inside fluid when jetting	$\mathrm{m.s^{-1}}$
c_L	Elastic compression waves velocity of solid	$\mathrm{m.s^{-1}}$
c_T	Elastic shear waves velocity of solid	$\mathrm{m.s^{-1}}$
D	Dilatation	-
E	Fatigue function	-
E_g	Fatigue function for general criterion	-
E_{DV}	Fatigue function for Dang Van criterion	-
E_0	Young's modulus of solid	Pa
E_t	Tangent modulus of solid	Pa
f	Wöhler line function	Pa
F	Yield function	Pa
H	Height of solid model	m
k	Fluid coefficient for water-hammer pressure	-
K	Bulk modulus	Pa
N	Number of cycles to failure	-
N_g	Number of cycles to failure according to general criterion	-
N_{DV}	Number of cycles to failure according to Dang Van criterion	-
N_{lim}	Number of cycles to failure lower limit	-
p	Contact pressure	Pa
p_f	Pressure inside fluid	Pa
p_{max}	Maximum contact pressure	Pa
p_{wh}	Water-hammer pressure	Pa
R	Droplet radius	m
R_{jet}	Radial location of jetting	m
s^a_{I}	First principal alternate deviatoric stress	Pa
s^a_{II}	Second principal alternate deviatoric stress	Pa
s^a_{III}	Third principal alternate deviatoric stress	Pa
t_m	Physical time at time step number m	s
T_c	Elapsed physical time of computation	s
T_{jet}	Jetting time	s
U	Elastic strain energy per unit volume	$\mathrm{J.m^{-3}}$
U_d	Distorsion strain energy per unit volume	$\mathrm{J.m^{-3}}$
U_v	Volumic strain energy per unit volume	$\mathrm{J.m^{-3}}$
V	Impact velocity	$\mathrm{m.s^{-1}}$
X	Hardening variable	Pa

Parameter	Description	Unit (ISO)
t	Physical time	s
x	Radial location	m
z	Vertical location	m
Re	Reynolds number	-
We	Weber number	-
α	First coefficient of Dang Van criterion	-
β	Second coefficient of Dang Van criterion	Pa
γ	Polytropic coefficient	-
$\Delta\sigma_{\mathrm{I}}^{(m,n)}$	First principal stress difference between time steps t_m and t_n	Pa
$\Delta\sigma_{\mathrm{II}}^{(m,n)}$	Second principal stress difference between time steps t_m and t_n	Pa
$\Delta\sigma_{\mathrm{III}}^{(m,n)}$	Third principal stress difference between time steps t_m and t_n	Pa
ε_H	Hydrostatic strain	-
λ	First Lamé coefficient	Pa
μ	Second Lamé coefficient or shear modulus	Pa
ν	Poisson's ratio	-
ρ_f	Density of fluid	$\mathrm{kg.m^{-3}}$
ρ_f^0	Initial density of fluid	$\mathrm{kg.m^{-3}}$
ρ_s	Density of solid	$\mathrm{kg.m^{-3}}$
σ_{-1}	Endurance limit under symmetrical alternate traction	Pa
σ_a	Stress amplitude	Pa
σ_a^g	Stress amplitude for general criterion	Pa
σ_{DV}	Dang Van equivalent stress	Pa
σ_a^{DV}	Dang Van equivalent stress amplitude	Pa
σ_{lim}	Stress amplitude upper limit	Pa
σ_H	Hydrostatic stress	Pa
σ_{VM}	Von Mises stress	Pa
$\sigma_{\mathrm{VM}}^{\mathrm{sign}}$	Signed Von Mises stress	Pa
σ_Y^0	Initial yield strength of solid	Pa
τ_{-1}	Endurance limit under symmetrical alternate torsion	Pa
τ^a	Alternate shear	Pa
τ_{I}^a	First principal alternate shear	Pa
τ_{II}^a	Second principal alternate shear	Pa
τ_{III}^a	Third principal alternate shear	Pa

Vectors

Parameter	Description	Unit (ISO)
$\mathbf{g}$	Gravitational constant field	$\mathrm{m.s^{-2}}$
$\mathbf{u}_s$	Displacement field inside solid	m
$\mathbf{v}_f$	Velocity field inside fluid	$\mathrm{m.s^{-1}}$

Tensors

Parameter	Description	Unit (ISO)
$\mathbf{1}$	identity matrix	-
$\mathbf{e}$	Deviatoric strain	-
$\mathbf{s}$	Deviatoric stress	Pa
$\mathbf{s}^a$	Alternate deviatoric stress	Pa
$\mathbf{s}^m$	Mean deviatoric stress	Pa
$\boldsymbol{\varepsilon}_s$	Strain field inside solid	-
$\boldsymbol{\varepsilon}^e$	Elastic part of strain field	-
$\boldsymbol{\varepsilon}^p$	Plastic part of strain field	-
$\boldsymbol{\sigma}_s$	Cauchy stress field inside solid	Pa
$\boldsymbol{\sigma}^{(m)}$	Cauchy stress at time step t_m	Pa
$\Delta\boldsymbol{\sigma}^{(m,n)}$	Stress difference between time steps t_m and t_n	Pa
$\mathbb{H}^{ep}$	Elastoplastic tangent modulus	Pa

1 Introduction

Hydraulic turbines can undergo severe damage during operation, because of low quality water or detrimental flow conditions. Damage induces maintenance costs and power production losses, and can also endanger safety of installations. Hydropower plants operators and turbine manufacturers are interested in extending overhaul periods by reducing damage intensity and protecting turbine components with surface treatments, but accurate and reliable prediction of damage is however missing. The present work is related to the erosion arising from repeated impacts of high speed water droplets on specific parts of Pelton turbines. Indeed for high head Pelton units, the jet of water is composed of a liquid core surrounded by droplets. Observations show that regions of impact of these droplets exhibit specific erosion patterns. First, the erosion mechanism is described, which allows to highlight the most important phenomena involved in the generation of damage. Then, numerical simulations are performed. They consist of the impact of a water droplet on a metallic structure, with an erosion post-processing.

2 Droplet impact erosion

This part explains the mechanism responsible for the wear of metallic structures by water droplets impingement. Firstly, the mechanisms happening into the droplet in case of impact are presented, like the “water-hammer" pressure and waves propagation. The maximum pressure on the wall appears when side jets emerge from the droplet. The pressure drop on the top of the droplet can induce cavitation. Then, the erosion mechanism itself inside the solid is presented. These mechanisms may be split into two groups : the damages acting at macroscopic scale, then the mesosopic ones, such as intergranular cracks propagation leading to grain removal or tilting. This last case produces pits on the surface.

2.1 Liquid-solid impact

2.1.1 Waves propagation

According to Haller and Li [1, 2], when a small diameter and high velocity water droplet impacts a rigid flat target, viscous effects and surface tension can be neglected. Indeed, for a droplet radius $R = 0.1$ mm and initial velocity $V = 500$ m.s^{-1}, Reynolds number is Re = 50′000 and Weber number is We = 350′000 [1]. Numerical results from Haller [1] show almost constant temperature, so convective heat transfert is not involved in the fluid motion. Therefore, the fluid behaviour is driven by inertial effects and Euler equations can be considered for numerical simulations. After impact, a shock wave starts moving from the contact zone and propagates along the droplet lateral free surface. This wave follows an unobservable triple point, near the contact edge. Field and Haller [3, 1] build the shock front with the geometric principle of Huygens-Fresnel. The front is the envelope of wavelets created by successive edges of the contact (Figures 1.a and 1.b). The volume defined by the wave front and the contact area is highly compressed (Figure 1.a).

Concerning the solid body, the droplet impact induces two main types of waves : spherical waves propagate inside volume and Rayleigh waves on the surface. Spherical waves consist into longitudinal compression waves (P-waves), and transverse shear waves (S-waves). S-waves propagate slower than P-waves for most of metals. Those different features are illustrated on Figure 2. For linear elastic isotropic material, P-waves velocity c_L and S-waves veocity c_T are expressed in equation (1) with λ and

μ as the first Lamé coefficient and the second or the shear modulus respectively given in equation (2), with E_0 and ν respectively the Young's modulus and Poisson's ratio. ρ_s stands for the solid density.

$$c_L = \sqrt{(\lambda + 2\mu)/\rho_s} \qquad c_T = \sqrt{\mu/\rho_s} \tag{1}$$

$$\lambda = \frac{\nu E_0}{(1+\nu)(1-2\nu)} \qquad \mu = \frac{E_0}{2(1+\nu)} \tag{2}$$

2.1.2 Contact pressure and micro-jetting

During the impact of a fluid body on a solid target, the "water-hammer" p_{wh} pressure emerges at the center of the contact area. Field, Heymann, Kennedy and Li [4, 5, 6, 2] give it expression for a rigid solid body in equation (3) :

$$p_{\text{wh}} = \rho_f^0 c_f V \tag{3}$$

where ρ_f^0 is the initial fluid density, s stands for the compression wave velocity traveling in the droplet (cf. Figure 1.c) and V the normal impact velocity of the droplet. Haller, Heymann and Li [1, 5, 2] approximate s in these conditions and give another expression for p_{wh} with equation (4), where k is a liquid-dependant constant, whose value equals 2 for water, and c_f^0 stands for initial sound velocity in water at room temperature :

$$p_{\text{wh}} = \rho_f^0 c_f^0 V \left(1 + k\frac{V}{c_f^0}\right) \tag{4}$$

Surface tension has no impact on pressure response (cf. 2.1.1). Numerical results from Haller and Li [1, 2] show the pressure distribution following the contact area across the time. According to Field, Haller, Heymann and Lesser [4, 1, 5, 7], the maximum pressure p_{max} occurs exactly on the edge of the contact area (Figure 3.a). The moment the maximum value acts is not at the start of impingement, but when the shock wave overtakes the contact area. Then, compression with solid leads to jetting by lateral ejection of the fluid (Figures 1.c and 3.b). The maximum pressure locates at the jetting region. These two informations are contained in equation (5) where R_{jet} and T_{jet} are respectively the location and the time of jetting :

$$p_{\text{max}} = p(x = R_{\text{jet}}, t = T_{\text{jet}}) \tag{5}$$

The velocity of the jet can be far higher than the impact velocity V and even the ambient sound velocity c_f^0 (Figure 3.b). Unfortunately analytical expression for maximum pressure does not exist. Numerical results of Haller and Kennedy [1, 6] give respectively $p_{\text{max}} \simeq 2p_{\text{wh}}$ and $p_{\text{max}} \simeq 3p_{\text{wh}}$. However, Haller [1] suggests the time when jets form t_{jet} with the equation (6), where $\hat{c}_f$ stands for compression wave velocity inside the droplet when jetting :

$$T_{\text{jet}} = \frac{RV}{2\hat{c}_f^2} \tag{6}$$

2.1.3 Cavitation

According to Obreschkow [8], a shock wave traveling into a liquid core could induce cavitation. Indeed, Field [4] states that superposition of relaxation waves generates tensile stress into the fluid body, which can lead to cavitation phenomena. For $V = 110\ \text{m.s}^{-1}$ and $R = 5$ mm, experimental results from Obreschkow [8] show that impact creates a thousands of submillimetric gas bubbles in the hemisphere opposite the impact zone (cf. Figure 4). High impact velocity increases the risk of cavitation. However experimental results from Field [4] with $V = 110\ \text{m.s}^{-1}$ and $R = 5$ mm show a cavitation appearing to far from the solid target to cause direct damage. Cavitation will not be implemented in the following numerical simulations.

2.2 Erosion mechanism

2.2.1 Macroscopic scale

Baker [9] worked on droplet impingement erosion of steam turbines blades and splits erosion mechanism into three phases :

(i) The first phase is called “incubation period”. During this time no significant loss in mass is observed, but the surface condition changes and becomes more rough.

(ii) Then, the loss in mass increases almost linearly until the rate of erosion reaches it maximum value and becomes constant.

(iii) Finally, erosion rate diminishes, possibly again becomes constant, or zero in some cases.

These steps are illustrated on Figure 5.

2.2.2 Mesoscopic scale

A mesoscopic description of erosion mechanism is proposed by Kamkar and Luiset [10, 11] as the following steps :

1. The first impacts start to erode grain boundaries and generates pits between grains. Then, micro-cracks appear at the bottom of these pits.

2. Next, material is removed from surface by two damage modes : a) grain ejection which can produce triple joins, b) grain fracture.

3. After a larger number of impacts, neigbour grains support the same damage mechanism and are ejected or fractured (step 2.). Microckacks are intergranular type, which impairs the surface condition, and move in parallel to the surface and propagate in depth. Microvoids born on the surface. The damage zone can be larger than the droplet itself.

4. These defaults are amplified by fatigue.

Finally, erosion is driven by plastic deformation, hardening, intergranular cracks propagation and fatigue mechanism. The cyclic nature of the damage produces a digging by steps (Figure 6). Kong [12] proposes a more suitable description for grain-sized droplets, which does not correspond to the present work conditions.

3 Numerical simulation of droplet impact erosion

This section presents the 2D transient simulation of a water droplet impact on a non-rigid solid body. Then, a fatigue post-processing is performed to estimate the damage over time and therefore the life cycle. The solid sub-domain is computed by the *Finite Elements Method* (FEM) with the explicit dynamics code *EuroPlexus*® [13], which is developed jointly by the french *Commissariat à l'Énergie Atomique et aux Énergies Alternatives* (CEA) and the *European Commission / Joint Research Center* (EC/JRC). This code is suitable for highly non-linear explicit dynamics with erosion. Concerning the fluid sub-domain, *ASPHODEL* code is used. This in-house code developed by *Andritz Hydro* uses the *Smoothed Particle Hydrodynamics* method (SPH) and is efficient to treat free surfaces. The *Fluid-Structure Interaction* (FSI) is performed by the two-way coupling code developed by Nuñez-Ramirez [14], which is energy-conservative at the interface for same time-steps.

3.1 Numerical model features

The solid body consists of a rectangular shaped steel domain, with height H and width $2H$. To avoid waves reflection, $H > c_L T_c$, where T_c is the elapsed time after impact, and c_L the compression waves velocity defined in equation (1). The material considered is homogeneous, isotropic and perfectly bilinear elastoplastic with Young's modulus E_0, second tangent modulus E_t, Poisson's ratio ν, initial yield strength σ_Y^0 and density ρ_s. Only isotropic hardening is condidered. The water droplet is a full disc with a radius $R = 0.5$ mm and moves perpendicularly towards the solid with an impact velocity $V = 100$ m.s^{-1}. The fluid core has a density ρ_f^0 and an ambient sound velocity c_f^0, neither viscosity nor surface tension (see section 2.1.1). Because of the abcense of convective effect (cf. section 2.1.1), the fluid satisfies the Tait's equation of state (Macdonald [15]), which is isothermal given by equation (7) with a zero reference pressure, where p_f and ρ_f are respectively pressure and density inside fluid and γ stands for the polytropic coefficient. All of the material data are summed up in Table 1 and the model is represented on Figure 7.

$$p_f = \frac{\rho_f^0 (c_f^0)^2}{\gamma} \left[\left(\frac{\rho_f}{\rho_f^0} \right)^\gamma - 1 \right] \tag{7}$$

3.2 Droplet impact on a rigid target

Before FSI computation, a fluid computation is performed with the impact of droplet on a rigid wall, in order to understand the nature of loads involved on the solid body. Figure 8.a shows the maximum pressure $p_{\max} \approx 1.7$ GPa, which equals ten times water-hammer pressure calculated with equation (4) and datas from section 3.1, which give $p_{\text{wh}} = 170$ MPa. Maximal pressure locates at $x/R = 0.18$, which corresponds to [1] (see Figure 3). The impulse per unite area, which is calculated by time integration

of the pressure, gives a better qualitative idea of load intensity in fast transient dynamics, the load time being responsible for the deformation of surface. The spatial shape of the impulse gives a maximum value at the center of contact and fluctuations are observed at $x/R = 0.18$, because of the instability of signal due to the water ejection.

3.3 FSI computation

3.3.1 Governing equations

Quantities which are expressed for both fluid and solid are distinguished by a subscript $\square_f$ and $\square_s$ respectively. The displacement is $\mathbf{u}$, the velocity $\mathbf{v}$, stress $\boldsymbol{\sigma}$, strain $\boldsymbol{\varepsilon}$, density ρ, pressure p, identity matrix is noted $\mathbf{1}$, and $\mathbf{g}$ stands for gravitational acceleration.

The fluid dynamics is described by Euler equations (cf. section 2.1.1) and Tait's equation of state (cf. 3.1) in equation (8) :

$$\begin{cases} \dfrac{\partial \rho_f}{\partial t} + \nabla \cdot (\rho_f \mathbf{v}_f) = 0 \\ \dfrac{\partial (\rho_f \mathbf{v}_f)}{\partial t} + \nabla \cdot (\rho_f \mathbf{v}_f \otimes \mathbf{v}_f) + \nabla \cdot (p_f \mathbf{1}) = \rho_f \mathbf{g} \\ p_f = \dfrac{\rho_f^0 (c_f^0)^2}{\gamma} \left[\left(\dfrac{\rho_f}{\rho_f^0} \right)^\gamma - 1 \right] \end{cases} \tag{8}$$

Concerning the solid, the classical Cauchy momentum equation is used. Material is considered to be elastoplastic. Strain $\boldsymbol{\varepsilon}_s$ is splitted into an elastic part $\boldsymbol{\varepsilon}^e$ and a plastic part $\boldsymbol{\varepsilon}^p$. Lamé coefficients λ and μ are given in equation (2) for elastic behaviour. $F(\boldsymbol{\sigma}_s, X)$ stands for the yield function with the Von Mises stress as trial stress (described in equation (16)), $\mathbb{H}^{ep}(\boldsymbol{\sigma}_s, X)$ is the elastoplastic tangent modulus and X the isotropic hardening variable, which depends on the cumulated plastic strain. More detailed are supplied by Aune [16] about the constitutive relation.

$$\begin{cases} \nabla \cdot \boldsymbol{\sigma}_s + \rho_s \mathbf{g} = \rho_s \dfrac{\partial^2 \mathbf{u}_s}{\partial t^2} \\ \boldsymbol{\varepsilon}_s = \dfrac{1}{2} \left(\nabla \mathbf{u}_s + \nabla^{\mathrm{T}} \mathbf{u}_s + \nabla \mathbf{u}_s \cdot \nabla^{\mathrm{T}} \mathbf{u}_s \right) \\ \boldsymbol{\varepsilon}_s = \boldsymbol{\varepsilon}^e + \boldsymbol{\varepsilon}^p \\ \boldsymbol{\sigma}_s = \lambda \mathrm{Tr}\left[\boldsymbol{\varepsilon}^e\right] \mathbf{1} + 2\mu \boldsymbol{\varepsilon}^e \\ \mathrm{d}\boldsymbol{\sigma}_s = \mathbb{H}^{ep}(\boldsymbol{\sigma}_s, X) : \mathrm{d}\boldsymbol{\varepsilon}_s \\ F(\boldsymbol{\sigma}_s, X) = \sigma_{\mathrm{VM}} - (\sigma_Y^0 + X) \end{cases} \tag{9}$$

3.3.2 Useful physical quantities for fatigue analysis

The Cauchy stress tensor $\boldsymbol{\sigma}_s$ can be splitted into a spherical part, called "hydrostatic stress" σ_H defined in equation (10) and a deviatoric one $\mathbf{s}$ in equation (11) :

$$\sigma_H = \frac{1}{3} \mathrm{Tr}\left[\boldsymbol{\sigma}_s\right] \tag{10}$$

$$\mathbf{s} = \boldsymbol{\sigma}_s - \sigma_H \mathbf{1} \tag{11}$$

In a same way the strain tensor $\boldsymbol{\varepsilon}_s$ can be splitted into a spherical part, called "hydrostatic strain" ε defined in equation (12) and a deviatoric one $\mathbf{e}$ in equation (13) :

$$\varepsilon_H = \frac{1}{3}\mathrm{Tr}\left[\boldsymbol{\varepsilon}_s\right] \tag{12}$$

$$\mathbf{e} = \boldsymbol{\varepsilon}_s - \varepsilon_H \mathbf{1} \tag{13}$$

The total strain energy per unit volume U can be splitted into a part relative to volume change U_v and another relative to change of shape (distortion) U_d defined in equation (14). U_v is relative to spherical part of stress and strain, and U_d to respective deviatoric parts and are given in equation (15) :

$$U = \frac{1}{2}\boldsymbol{\sigma}_s : \boldsymbol{\varepsilon}_s = U_v + U_d \tag{14}$$

$$U_v = \frac{1}{2}\sigma_H \varepsilon_H \qquad\qquad U_d = \frac{1}{2}\mathbf{s} : \mathbf{e} \tag{15}$$

The deviatoric stress allows to define the Von Mises stress, which is a an euclidian norm of $\mathbf{s}$ in equation (16) :

$$\sigma_{\mathrm{VM}} = \sqrt{\frac{3}{2}\mathbf{s} : \mathbf{s}} \tag{16}$$

For infinitesimal strains, quadratic terms of $\boldsymbol{\varepsilon}_s$ from equation (9) are neglegted and strain tensor becomes the symmetrized gradient of displacement $\mathbf{u}_s$:

$$\boldsymbol{\varepsilon}_s \approx \nabla^{\mathrm{sym}} \mathbf{u}_s \tag{17}$$

The divergence of displacement stands for dilatation D and is linked to hydrostatic strain ε_H in equation (18) by using equation (17) into equation (12) :

$$D = \nabla \cdot \mathbf{u}_s = 3\varepsilon_H \tag{18}$$

For linear elastic and isotropic material, σ_H is proportioannly linked to hydrostatic strain ε_H by the bulk modulus K. By using equation (18) one gets a linear relation between hydrostatic stress σ_H and dilatation D in equation (19) :

$$\sigma_H = K\varepsilon_H = \frac{K}{3}D \qquad\qquad K = 3\lambda + 2\mu \tag{19}$$

Being a norm, Von Mises stress is a positive quantity. Let us define the signed Von mises stress $\sigma_{\text{VM}}^{\text{sign}}$ with the sign of hydrostatic stress in equation (20) :

$$\sigma_{\text{VM}}^{\text{sign}} = \text{sign}\,(\sigma_H)\sigma_{\text{VM}} = \frac{\sigma_H}{|\sigma_H|}\sigma_{\text{VM}} \tag{20}$$

3.3.3 Results

Using equation (1) with material data from Table 1 allows to obtain numerical values for velocities $c_L \approx 5820$ m.s^{-1} and $c_T \approx 3175$ m.s^{-1}, which are both higher than the ambient water sound velocity considered $c_f^0 = 1500$ m.s^{-1}. Propagation of compression waves is given by observing the evolution and distribution of pressure inside the droplet p_f. A negative pressure corresponds to tension, and a positive one to compression. Concerning the solid, hydrostatic stress σ_H defined in equation (10) can be used . Unlike p_f the sign convention of σ_H is the following : $\sigma_H > 0$ in regions subjected to traction and $\sigma_H < 0$ for compression. Indeed, equation (19) give a proportional relation between hydrostatic stress σ_H and dilatation D, with $K > 0$. Thus, hydrostatic stress describes the traction-compression state. For solids, shear waves act jointly to compression waves (cf. 2.1.1). They can be observed with the Von Mises stress σ_{VM} defined in equation (16). Indeed, shear is related to distortion, and σ_{VM} depends on the stress deviator $\mathbf{s}$ which defines distortion energy U_d in equation (15). As Von Mises stress stands for the shear intensity and hydrostatic stress gives information about the straction-compression state, the signed Von Mises stress defined in equation (20) gives both informations about shear and traction-compression and is useful to locate zones caring fatigue load and potential crack initiation and propagation. Indeed high shear can lead to cracks initiation and a traction state tends to open them (and a compression state to close). Figure 9 shows both hydrostatic and Von Mises stresses acting in the structure for three different times after impact. By observing those quantities, P-waves and S-waves front appear to show the velocity difference. However, the front gap between P and S-waves is not clear, due to the nature of load. Indeed, droplet impingement does not act like a proper impact, as seen on Figure 8, the pressure depends on time and especially on space too. Then, it maximum value is reached when microjets form, thus on contact boundary. Finally, contact area growths faster than compressions waves inside fluid during the first moments of the impact, which generates other fast moving loading sources. This complex load induces mixed moving stress, such as traction/compression and shear at the same time, and the location of loading sources moves fast. Nevertheless, the travelling of a traction-compression wave is observed, which shows a general overview of the zones caring high stresses in term of fatigue. Analysis of hydrostatic and Von Mises stresses allows to globally estimate the type of load inside the solid volume. For a solid region near the surface, the different times of Figure 9 show a change of sign for hydrostatic stress. Indeed, hydrostatic stress in Figure 10.a shows that this region is subject to a traction-compression cycle during the droplet impingement. Signed Von Mises stress defined in equation (20) is given on Figure 11 at the time of jetting. It magnitude give the shear intensity and it sign shows the traction or compression state. Zones where high discontinuities stand are subject to combined effect of both traction/compression and shear, which are important quantities for crack initiation and propagation.

Results show absence of plasticity due to low stress intensity compared to the yield stress (Figures 9, 10 and 11). This assertion is well checked by observing the cumulated plastic strain, which is zero. Low stresses and absence of plasticity head to high cycle fatigue domain (plasticity and hardening leading

to oligocyclic fatigue domain). This information is important for the choice of fatigue criterion.

3.4 Fatigue analysis

3.4.1 Erosion program

The result of simulations allow to define the eroded zones for a given fatigue criteria. After a transient computation, each element of the mesh contains a stress, strains, displacement, etc. history. These physical quantities are used to define a fatigue criterion, which produces a condition to select which elements of the mesh are eroded and should be removed. This condition is called "fatigue function" and consists into a dimensionless quantity $E \in [0, 1]$. The condition of erosion being $E = 1$, and $E = 0$ corresponding to a virgin element. A fatigue criterion needs a number of load cycles N_{lim} as input, which corresponds to lower limit for non-eroded elements. Fatigue criterion give the opportunity to predict how many identical load cycles N each element can carry before failure. If $N \leq N_{\text{lim}}$, i.e $E = 1$, the element is eroded. This method is a predicting one, and saves a lot of time, because only one load cycle is simulated and not N_{lim}. After removing eroded elements of the mesh, a new FSI interface is computed and another simulation is launched for another number of cycles. The main procedure is detailed on Figure 12. This paper presents only one FSI computation without loop.

3.4.2 Fatigue datas

Generally, resistance to fatigue is checked with a S-N curve such as the Wöhler line (Figure 13), which depends on the material. For a given stress amplitude σ_a, the corresponding number of cycles to failure N is found. If $N \leq N_{\text{lim}}$, fatigue cracking initiates. S-N curve representing a bijection, let call the function f which give the stress corresponding to a number of cycles, and f^{-1} it reverse function. The corresponding stress for the number of cycles lower limit N_{lim} is called σ_{lim} in equation (21) :

$$\begin{cases} \sigma_{\text{lim}} = f(N_{\text{lim}}) \\ N = f^{-1}(\sigma_a) \end{cases} \tag{21}$$

The fatigue function is then calculated as the ratio between the stress amplitude σ_a and the stress limit σ_{lim} in equation (22).

$$E = \frac{\sigma_a}{\sigma_{\text{lim}}} \tag{22}$$

If E exceeds 1, it value is usually brought back to 1 for more relevance. Indeed, from $E \geq 1$, the element concerned is damaged, regardless of the value of E. Note that E is relative to the chosen number of cycles N_{lim}. The stress amplitude σ_a is obtained by a fatigue criteria, which is the topic of the next section.

3.4.3 General fatigue criterion

A large number of fatigues criteria are found in litterature. A list is provided by Chamat and Weber [17, 18]. Fatigue criteria can be spitted into four main types : energetic, global, critical plan and empiric.

The main difficulty is to define the stress amplitude σ_a. For multiaxial fatigue, stresses $\boldsymbol{\sigma}_s$ are described by several components σ_{ij}, and σ_a depends on all these quantities. As a first try, a general and simple criteria is considered. The amplitude stress σ_a is computed with principal stresses, because they give the maximum stress state in the material. The amplitude is got by using the difference between the maximal (or minimal) and the mean value. Taking the half-difference between maximum and minimum values is faster. These two quantities are found by sweeping and comparing all the values. As principal axis could move too much, comparing a principal stress at a time step t_m with another time steps t_n should be impossible because they are not expressed in the same basis. The solution is to compare stresses in the absolute basis first, and then, calculating eigenvalues of stress tensor to get the corresponding principal stresses. For two time steps t_m and t_n with respective Cauchy stress tensors $\boldsymbol{\sigma}^{(m)}$ and $\boldsymbol{\sigma}^{(n)}$, one defines the difference stress tensor $\Delta\boldsymbol{\sigma}^{(m,n)}$ for the couple (t_m, t_n) in equation (23) :

$$\Delta\boldsymbol{\sigma}^{(m,n)} = \boldsymbol{\sigma}^{(m)} - \boldsymbol{\sigma}^{(n)} \qquad \text{with } m \neq n \tag{23}$$

Then, computing eigenvalues of $\Delta\boldsymbol{\sigma}^{(m,n)}$ gives the principal difference stresses $\Delta\sigma_{\mathrm{I}}^{(m,n)}$, $\Delta\sigma_{\mathrm{II}}^{(m,n)}$, $\Delta\sigma_{\mathrm{III}}^{(m,n)}$. Finally, the range $\Delta\sigma$ is got by using the Rankine criterion (uniform norm) to these stresses, and the stress amplitude σ_a^g is the half of the range in equation (24) :

$$\Delta\sigma = \|\Delta\boldsymbol{\sigma}^{(m,n)}\|_\infty = \sup_{\substack{m,n \\ m\neq n}} \left\{ \left|\Delta\sigma_{\mathrm{I}}^{(m,n)}\right|, \left|\Delta\sigma_{\mathrm{II}}^{(m,n)}\right|, \left|\Delta\sigma_{\mathrm{III}}^{(m,n)}\right| \right\} \qquad \sigma_a^g = \frac{\Delta\sigma}{2} \tag{24}$$

Finally, the number of cycles to failure N_g corresponding to the stress amplitude σ_a^g is got by the fatigue law given by the Wöhler curve defined in equation (21). The fatigue function is then computed with equation (22). In this case, fatigue function is also called “damage indicator” or “failure flag”.

3.4.4 Dang Van 2 fatigue criterion

The next criterion chosen is the second version of Dang Van criterion [19]. The fatigue function E_{DV} is given in equation (25) :

$$E_{\mathrm{DV}} = \sup_t \left\{ \frac{\tau^a(t) + \alpha\sigma_H(t)}{\beta} \right\} \tag{25}$$

where $\sigma_H(t)$ is hydrostatic stress (defined in equation (10)), $\tau^a(t)$ stands for alternate shear and α, β are two coefficients depending on the material given in equation (26) :

$$\alpha = 3\left(\frac{\tau_{-1}}{\sigma_{-1}} - \frac{1}{2}\right) \qquad \beta = \tau_{-1} \tag{26}$$

where σ_{-1} and τ_{-1} are respectively the endurance limit under symmetrical alternate traction and torsion. As measures for τ_{-1} are difficult to provide, the approximative value $\tau_{-1} = \sigma_{-1}/\sqrt{3}$ is considered,

because this value establishes an adequat approximation for most of stainless steels. This choice satisfies the validity condition fot the criterion $\tau_{-1}/\sigma_{-1} > 1/2$. It can be noted that α no longer depends on the material. One defines the alternate deviatoric stress $\mathbf{s}^a(t)$ and the time average deviatoric value $\mathbf{s}^m$ of $\mathbf{s}(t)$ in equation (27) :

$$\mathbf{s}^a(t) = \mathbf{s}(t) - \mathbf{s}^m \qquad \mathbf{s}^m = \frac{1}{T_c}\int_0^{T_c} \mathbf{s}(t)\mathrm{d}t \tag{27}$$

The alternate shear $\tau^a(t)$ is got by applying the Tresca criterion over the alternate deviatoric stress, which is the uniform norm of the maximum shears in equation (28). Planes of maximum shearing stress are inclined at 45° with respect to the planes of principal stress, and principal axis of $\mathbf{s}(t)$ are the same as $\boldsymbol{\sigma}(t)$ at each point :

$$\tau^a(t) = \text{Tresca}\left\{\mathbf{s}^a(t)\right\} = \sup_K \left\{\tau_K^a(t)\right\} \tag{28}$$

where principal shears $\tau_K^a(t)$ are given as function of eigen values $s_{\mathrm{I}}^a(t)$, $s_{\mathrm{II}}^a(t)$, $s_{\mathrm{III}}^a(t)$ of $\mathbf{s}^a(t)$ described in equation (29) :

$$\tau_{\mathrm{I}}^a(t) = \frac{\left|s_{\mathrm{II}}^a(t) - s_{\mathrm{III}}^a(t)\right|}{2} \qquad \tau_{\mathrm{II}}^a(t) = \frac{\left|s_{\mathrm{III}}^a(t) - s_{\mathrm{I}}^a(t)\right|}{2} \qquad \tau_{\mathrm{III}}^a(t) = \frac{\left|s_{\mathrm{I}}^a(t) - s_{\mathrm{II}}^a(t)\right|}{2} \tag{29}$$

Finally, the alternate shear is got in equation (30) :

$$\tau^a(t) = \frac{1}{2}\sup\left\{\left|s_{\mathrm{I}}^a(t) - s_{\mathrm{II}}^a(t)\right|, \left|s_{\mathrm{II}}^a(t) - s_{\mathrm{III}}^a(t)\right|, \left|s_{\mathrm{III}}^a(t) - s_{\mathrm{I}}^a(t)\right|\right\} \tag{30}$$

One defines commonly the Dang Van equivalent stress σ_{DV} in equation (31) :

$$\sigma_{\mathrm{DV}} = \sup_t \left\{\tau^a(t) + \alpha\sigma_H(t)\right\} \tag{31}$$

In this study, $\sigma_{-1} = \sigma_{\mathrm{lim}}$, so the fatigue function can be put in the same form as section 3.4.2 in equation (32) whith the corresponding stress amplitude σ_a^{DV} :

$$E_{\mathrm{DV}} = \frac{\sigma_a^{\mathrm{DV}}}{\sigma_{\mathrm{lim}}} \qquad \text{with } \sigma_a^{\mathrm{DV}} = \sqrt{3}\sigma_{\mathrm{DV}} \tag{32}$$

Finally, the number of cycles to failure N_{DV} corresponding to the stress amplitude σ_a^{DV} is got by the fatigue law given by the Wöhler curve defined in section 3.4.2. In this case, fatigue function is also called “damage indicator” or “failure flag”.

3.4.5 Results and discussion

Results of fatigue analysis according the two criteria (general and Dand Van) are detailed in this section. Each figure shows quantities relative to fatigues (stress amplitude, number of cycles to failure and damage indicator) for both criteria. The left side of isovalues map is dedicated to general criteria (cf. section 3.4.3) and right side to Dang Van criterion (cf. section 3.4.4). Figure 14 shows the stress amplitude for both criteria : σ_a^g defined in equation (24) for general criterion and σ_a^{DV} in equation (32) for Dang Van criterion. Figure 15 shows the corresponding number of cycles to failure for both criteria (N_g and N_{DV}) and Figure 16 the damage indicator for both criteria (E_g and E_{DV}) considering an input $N_{\mathrm{lim}} = 10$ Mcycles where eroded elements are removed from the mesh, i.e. those where $E \geq 1$ or $N \leq N_{\mathrm{lim}}$.

General criterion gives a maximum value of $\sigma_a^g = 83$ MPa, and Dang Van criterion gives $\sigma_a^{\mathrm{DV}} = 57$ MPa. The first elements break from $N_g = 4$ Mcycles according to general criterion, and $N_{\mathrm{DV}} = 8$ Mcycles to Dang Van criterion. In other words, it takes N impacts with same conditions to erode each element. With both criteria, eroded zone is enveloping around the jetting area, marked on Figures 14, 15 and 16. The damage shape is then a crown surrounding the jetting zone. These zones are subjected to high stress difference according to general criterion and high combined shear and hydrostatic stress according to Dang Van criterion, but eroded zones are diferent. The first difference is the size of damage zone : general criterion generates a wider and deeper damage than Dang Van criterion. The other difference concerns the interface layer. Dang Van criterion preserves the first layer of elements, which is quite unbroken, where $N_{\mathrm{DV}} \approx 1$ Gcycles $\gg N_{\mathrm{lim}}$ (Figure 15). The convergence of mesh were checked and we observe this virgin layer systematically. The reason of these differences is the formulation of those criteria. Indeed they do not consider the same physical quantities for the fatigue analysis. General criterion focuses on the highest different stress state, principal stresses giving the maximum stress state in each point without splitting it into particular stresses such as traction or shear, which are important for fatigue analysis. Otherwise, Dang Van criterion considers and dissociates shear on one hand and traction-compression on the other. It is highly sure that this material layer will break during the next droplet impact, ie for $N = N_{\mathrm{lim}} + 1$, which is quite equivalent to $N \approx N_{\mathrm{lim}}$, because $N_{\mathrm{lim}} \gg 1$, making this layer slightly irrelevant.

These results are generated considering strong assumptions : there is no surface change during the N cycles and the surface is cleaned between each cycle, thus water is removed before the next impingement, and shall not influence the next one. Therefore, a small number of cycles N_{lim} must be chosen for realistic model, because a different surface would certainly modify the physics of impact, such as stress concentration inside solid or higher fluid compression. Nevertheless, N_{lim} must be high enough to agree with high cycle fatigue theory.

4 Conclusion

When high velocity droplet with small diameter impacts a rigid target, interaction is driven by inertial effects. Thus, viscous forces and surface tension can be neglected and Euler equations are relevant to represent the fluid behaviour. By inertial effect, water-hammer pressure appears at the center of the contact area, but maximal pressure locates on the contact edge. A compression wave travels inside the droplet, starting from the contact zone. When wave front overtakes contact area, microjets appear near the surface by compression effect. Concerning the structure, erosion is due to fatigue cracking.

First, material grains are weakened during an "incubation" phase. After a large number of impacts, micro-cracks emerge and lead to ejection or fracture of grains, what is called "amplification" phase. Numerical simulations are performed subsequently. The droplet impact on a rigid target allows to find the pressure peak and thanks to the impulse, to locate the most loaded zone of the interface. Then, a 2-way coupling FSI computation is build, which gives a general overview of the fatigue mechanism by observing hydrostatic and Von Mises stresses. Finally, a fatigue analysis is considered with two different criteria : a general one and the Dang Van criterion. This study supplies a forecasting approach by giving informations on structure lifetime. It exposes a crown-shaped damage zone, which locates around jetting zone, showing the influence of microjets on the mechanism of erosion by water impingement. While both criteria indicate the same location of erosion, general criterion produces a larger and deeper damage than Dang Van criterion. This difference arises from the different quantities considered by each criterion for stress amplitude. These first results will be a strong basis for a sensitivity analysis on main impact parameters (droplets diameter and velocity). It is also planned to investigate the influence of a thin water layer set on the solid surface to mimic the wet environment, and a multi-layer material to take into account the coated surface of Pelton buckets.

Acknowledgement

The research leading to these results has received funding from the European Community's Seventh Framework Programme (FP7 / 2007-2013) under Grant Agreement 608393 "PREDHYMA".

References

[1] K. K. Haller, Y. Ventikos, D. Poulikakos. *Computational study of high-speed liquid droplet impact*, Journal of applied physics, 2002, 92, 2821-2828

[2] R. Li, H. Ninokata, M. Mori. *A numerical study of impact force caused by liquid droplet impingement onto a rigid wall*, Progress in Nuclear Energy, 2011, 53,7, 881-885

[3] J.E. Field. *ELSI Conference: invited lecture: Liquid impact: theory, experiment, applications*, Wear, 1999, 233-235, 1-12

[4] J.E. Field, J.-J. Camus, M. Tinguely, D. Obreschkow, M. Farhat. *Cavitation in impacted drops and jets and the effect on erosion damage thresholds*, Wear, 2012, 290-291, 154-160

[5] F.J. Heymann. *High-speed impact between a liquid drop and a solid surface*, Journal of Applied Physics, 1969, 40, 5113-5122

[6] C. F. Kennedy, J. E. Field. *Damage threshold velocities for liquid impact*, Journal of Materials Science 2000, 35, 5331-5339

[7] M.B. Lesser. *Thirty years of liquid impact research: a tutorial review*, Wear, 1995, 186, 28-34

[8] D. Obreschkow, N. Dorsaz, P. Kobel, A. de Bosset, M. Tinguely, J. Field, M. Farhat. *Confined Shocks inside Isolated Liquid Volumes - A New Path of Erosion ?*, Physics of Fluids, 2011, 23

[9] D. W. C. Baker, K. H. Jolliffe and D. Pearson. *The Resistance of Materials to Impact Erosion Damage*, Philosophical Transactions of the Royal Society of London A: Mathematical, Physical and Engineering Sciences, The Royal Society, 1966, 260, 193-203

[10] N. Kamkar, F. Bridier, P. Jedrzejowski, P. Bocher. *Water droplet impact erosion damage initiation in forged Ti-6Al-4V*, Wear, 2015, 322-323, 192-202

[11] B. Luiset, F. Sanchette, A. Billard, D. Schuster. *Mechanisms of stainless steels erosion by water droplets*, Wear, 2013, 303, 1-2, 459-464

[12] M.C. Kong, D. Axinte, W. Voice. *Aspects of material removal mechanism in plain waterjet milling on gamma titanium aluminide*, Journal of Materials Processing Technology, 2010, 210, 573-584

[13] CEA/DEN/SEMT/DYN *EuroPlexus. A computer program for the finite element simulation of fluid-structure systems under dynamic loading*, Users manual, 2002

[14] J. Nuñez-Ramirez, J.-C. Marongiu, M. Brun, A. Combescure. *A partitioned approach for the coupling of SPH and FE methods for transient non?linear FSI problems with incompatible time-steps*, International Journal for Numerical Methods in Engineering, 2017

[15] J. R. Macdonald. *Some Simple Isothermal Equations of State*, Rev. Mod. Phys., American Physical Society, 1966, 38, 669-679

[16] V. Aune, F. Casadei, G. Valsamos, T. Børvik. *Formulation and Implementation of the VPJC Material Model in EuroPlexus*, Publications Office of the European Union, 2016

[17] A. Chamat. *Prévivion de la durée de vie en fatigue des roues ferroviaires sous sollicitations multiaxiales proportionnelles et non-proportionnelles*, PhD Thesis, Laboratoire de Fiabilité Mécaniqu, École Nationale d'Ingénieurs de Metz, 2005

[18] B. Weber. *Fatigue multiaxiale des structures industrielles sous chargement quelconque*, PhD Thesis - Laboratoire de Mécanique des Solides - Institut National des Sciences Appliquées de Lyon, 1999

[19] K. Dang Van, B. Griveau, O. Message. *On a new multiaxial fatigue limit criterion: theory and application*, Biaxial and Multiaxial Fatigue, EGF Publication, 1989, 3, 479-496

Tables

Table 1: Material data for numerical simulations.

Solid		Fluid	
ρ_s	7700 kg.m^{-3}	ρ_f^0	1000 kg.m^{-3}
E_0	200 GPa	c_f^0	1500 m.s^{-1}
E_t	20 GPa	γ	7
σ_Y^0	560 MPa		
ν	0.288		

Figures

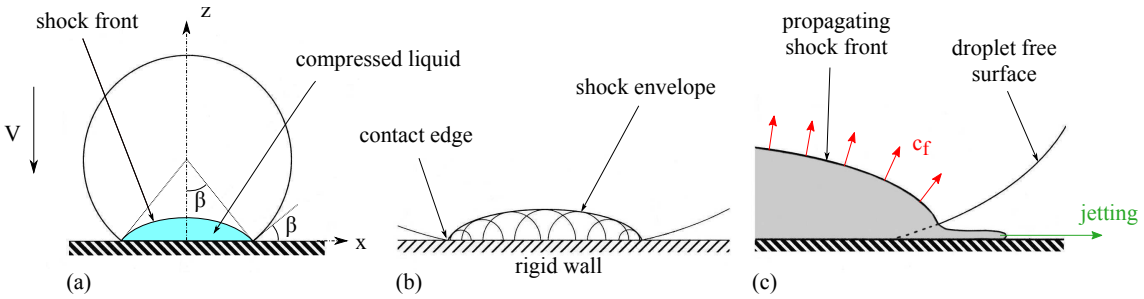

Figure 1: Impact of a spherical droplet on a rigid wall. **(a)** Shock front and highly compressed volume. **(b)** Geometric construction of the waves front. **(c)** Born of lateral micro-jets. (Haller [1]).

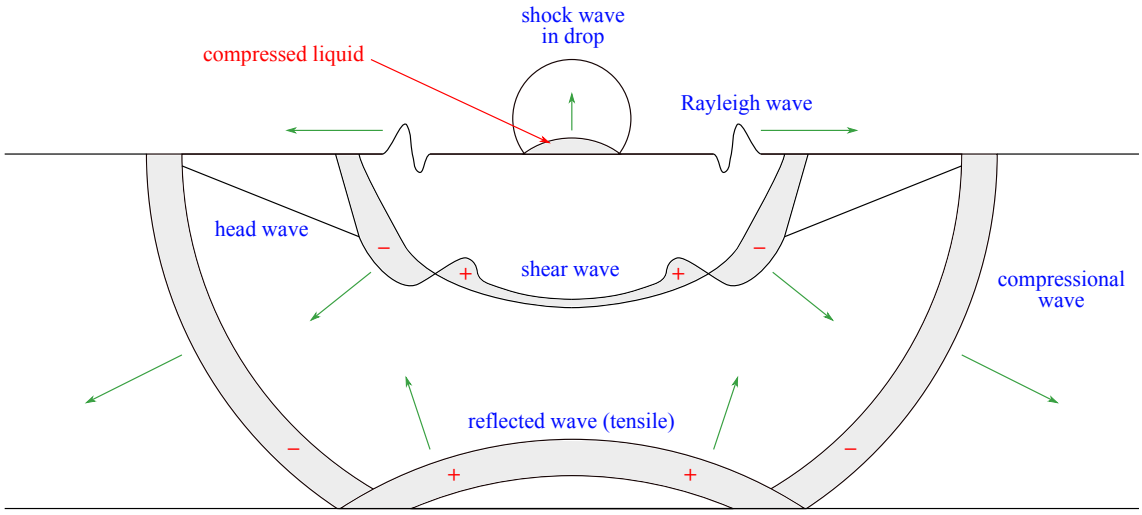

Figure 2: Different types of waves involved when a water droplet impacts an elastic, isotropic, and homogeneous solid body. Arrows show the direction to which the waves propagate. Signs (+/-) indicate the relative amplitude of particle motion inside shaded widths.

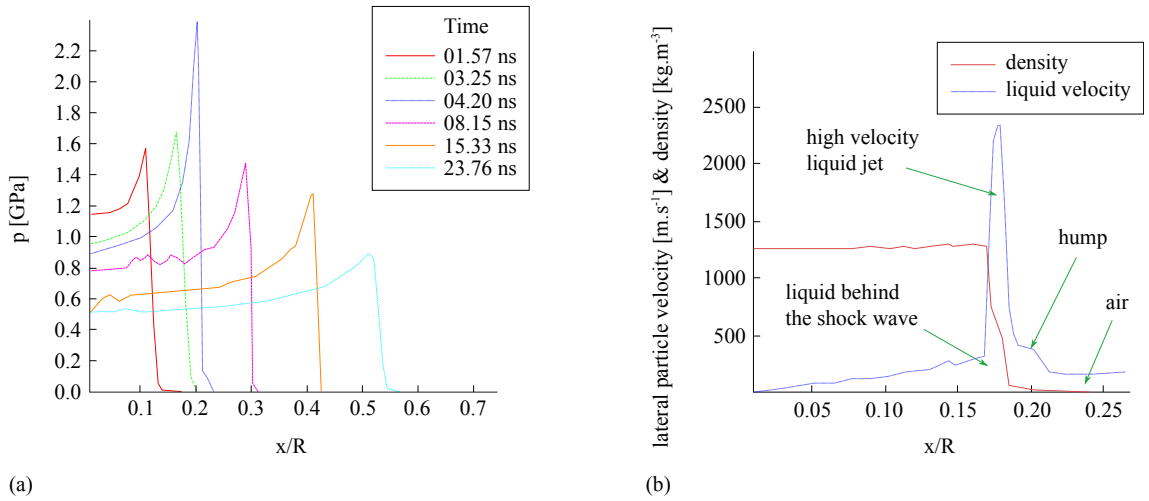

Figure 3: **(a)** Spatial distribution of contact pressure for several times after impact ($R = 0.1$ mm, $V = 500$ m.s^{-1}). **(b)** Radial velocity and density at the contact zone when jetting. Fluid radial velocity at contact zone (dotted line) shows clearly the jetting initialization at peak location (Haller [1]).

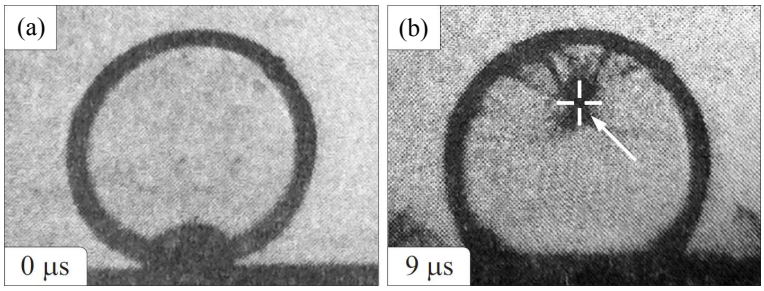

Figure 4: Cavitation inside a water droplet impacting on a rigid target ($V = 110$ m.s^{-1}, $R = 5$ mm). Dark regions represent high pressure / relaxation. **(a)** When impacting. **(b)** After waves reflection on the upper edge. Arrow locates the cavitation formation. (Obreschkow [8]).

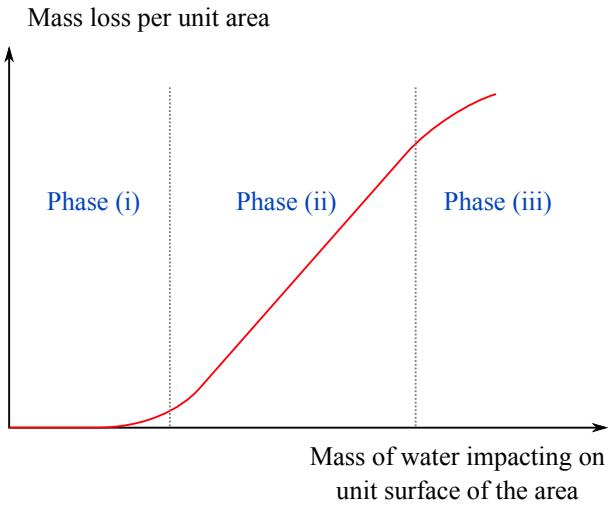

Figure 5: Typical erosion curve (Baker [9]).

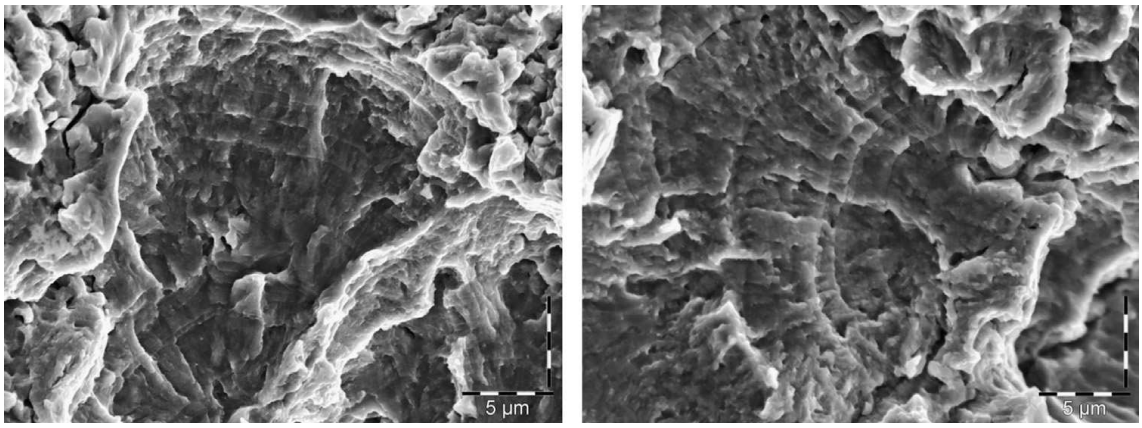

Figure 6: Damage resulting from repeated droplet impacts on stainless steel (Luiset [11]).

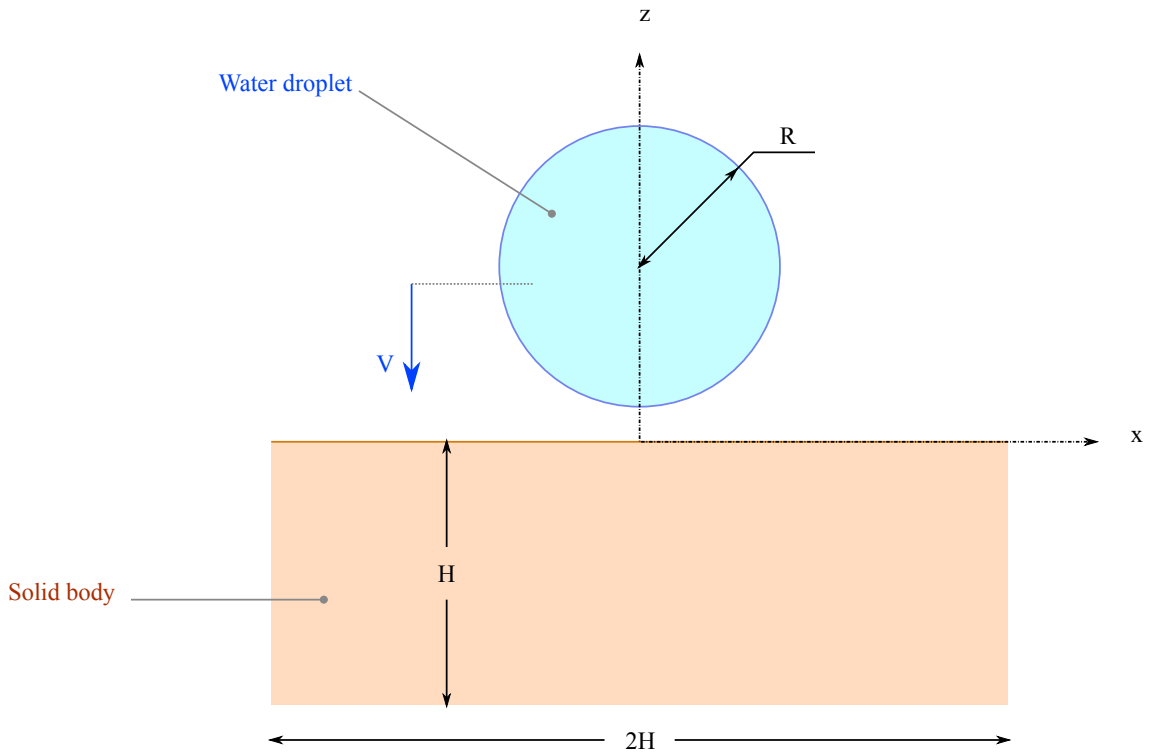

Figure 7: Representation of the numerical model.

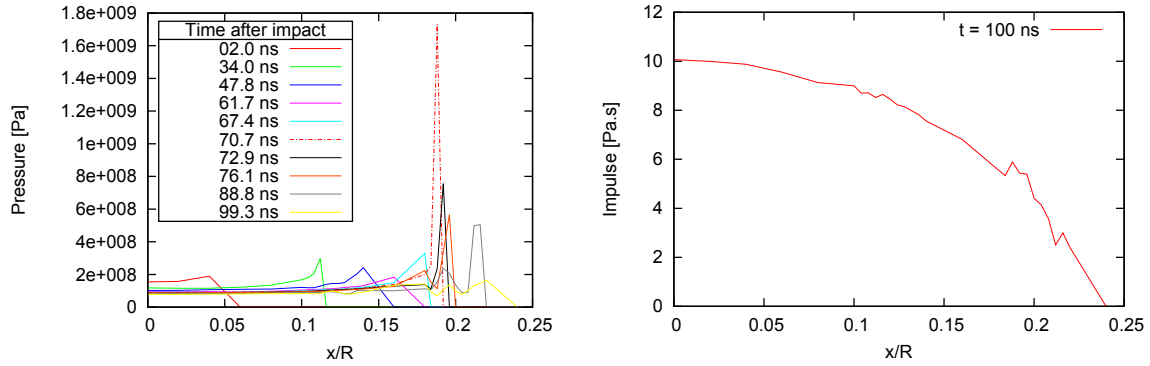

(a) (b)

Figure 8: Load distribution on rigid wall caused by droplet impingement ($R = 0.5$ mm, $V = 100$ m.s^{-1}). Location $x/R = 0$ corresponds to the center of the droplet. **(a)** Pressure distribution on the wall for ten representative times after impact. **(b)** Impulse distribution per unit area on the wall at $t = 100$ ns after impact.

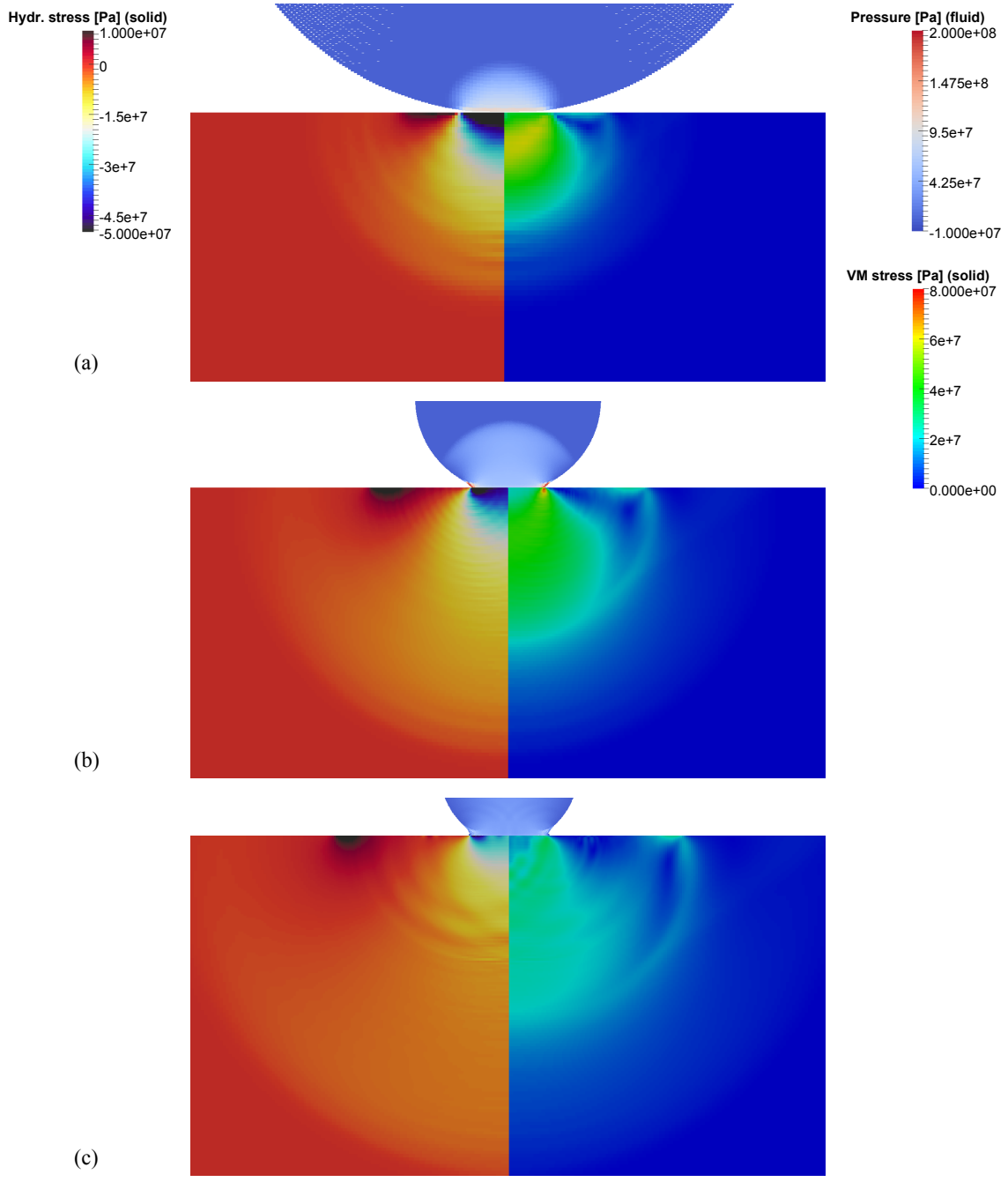

Figure 9: Pressure inside fluid, hydrostatic and Von Mises stress (respectively left and right) inside solid for several times after impact. **(a)** t = 60 ns. **(b)** t = 260 ns. **(c)** t = 440 ns. Same isovalue scale for every view, different view scales.

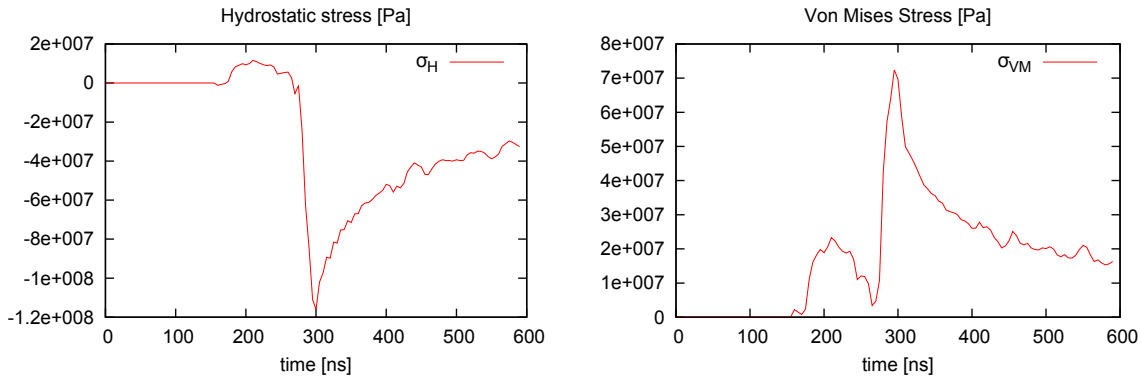

(a) (b)

Figure 10: Stresses at $x = 0.1425$ mm, $z = -2.5$ μm vs. time. Droplet impacts the solid at $t = 130$ ns **(a)** Hydrostatic stress. **(b)** Von Mises stress.

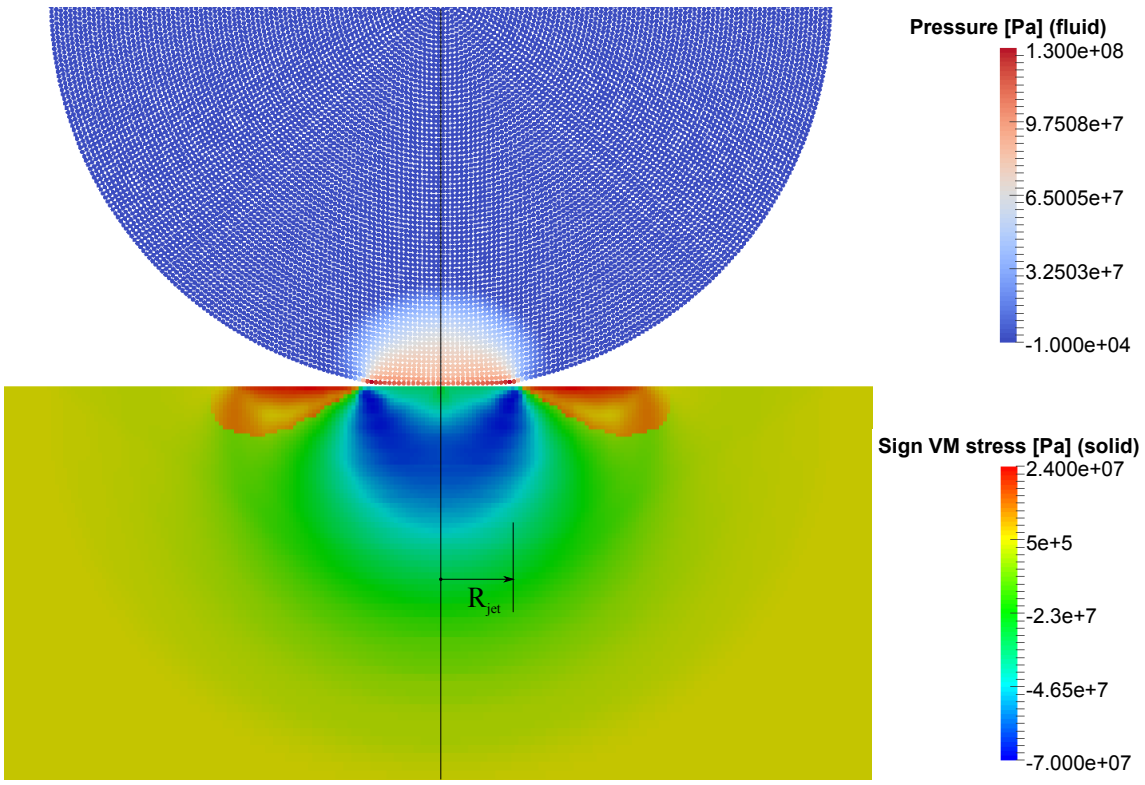

Figure 11: Signed Von Mises Stress $\sigma_{\mathrm{VM}}^{\mathrm{sign}}$ inside solid and pressure inside fluid at jetting time $T_{\mathrm{jet}} \approx$ 100 ns after impact.

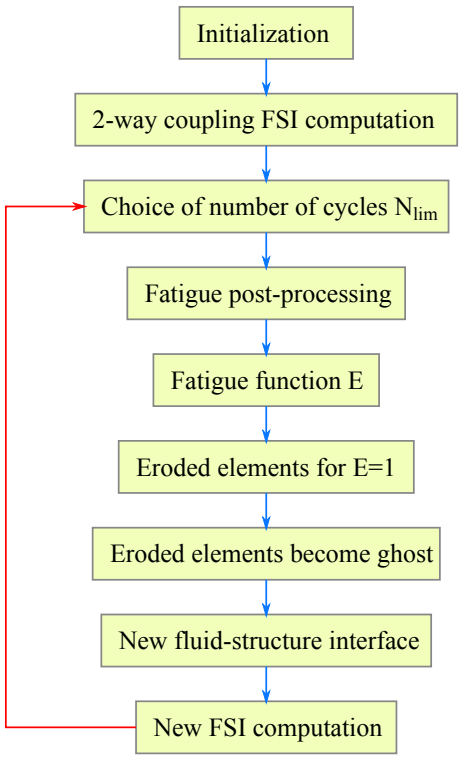

Figure 12: Erosion simulation procedure.

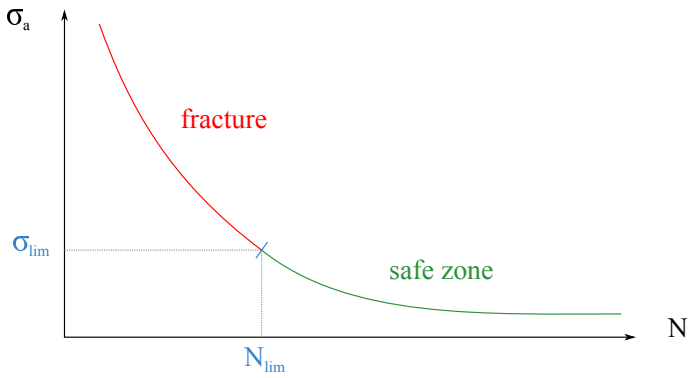

Figure 13: Wöhler line.

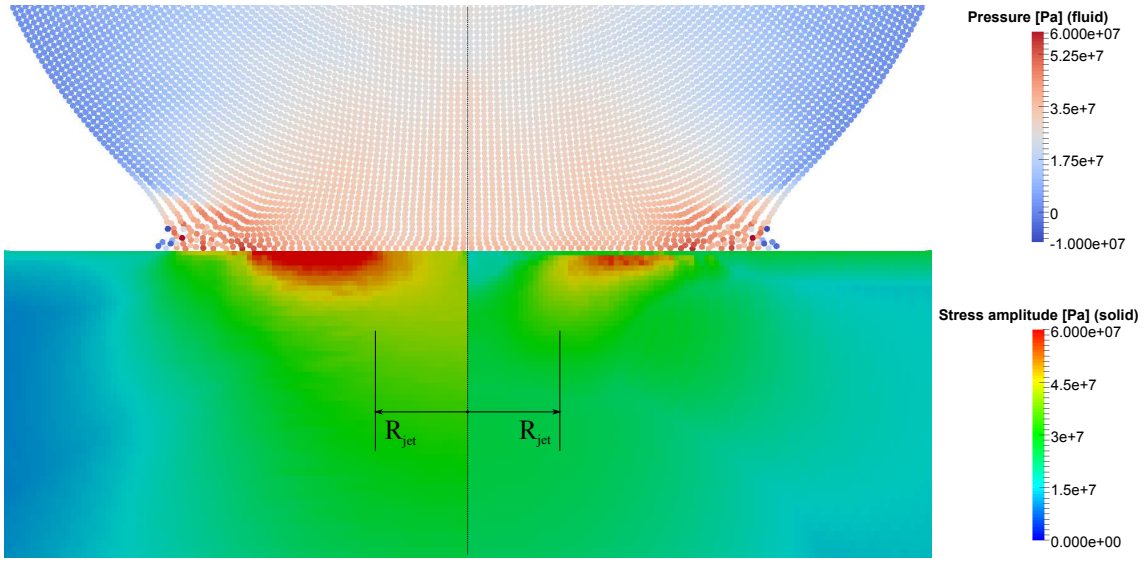

Figure 14: Pressure inside fluid p_f and stress amplitude inside solid at $t = 460$ ns after impact according to general criterion σ_a^g (left) and Dang Van criterion σ_a^{DV} (right). Marks indicate the jetting location at $x = \pm R_{\mathrm{jet}}$.

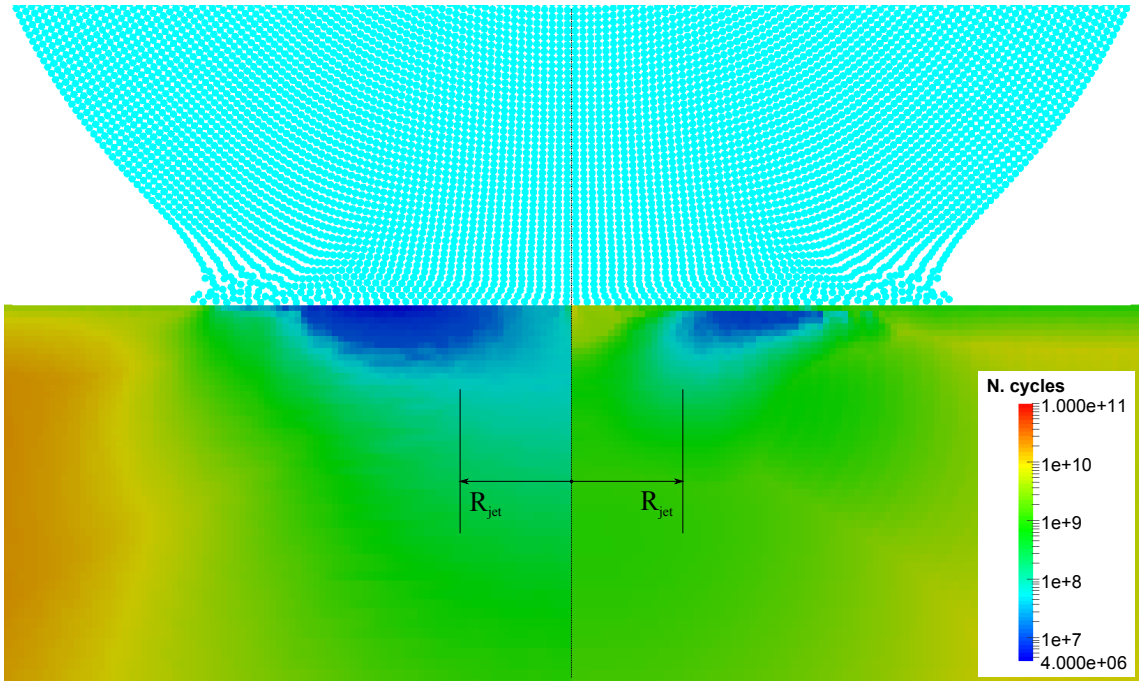

Figure 15: Number of cycles to failure inside solid at $t = 460$ ns after impact according to general criterion N_g (left) and Dang Van criterion N_{DV} (right). Marks indicate the jetting location at $x = \pm R_{\mathrm{jet}}$.

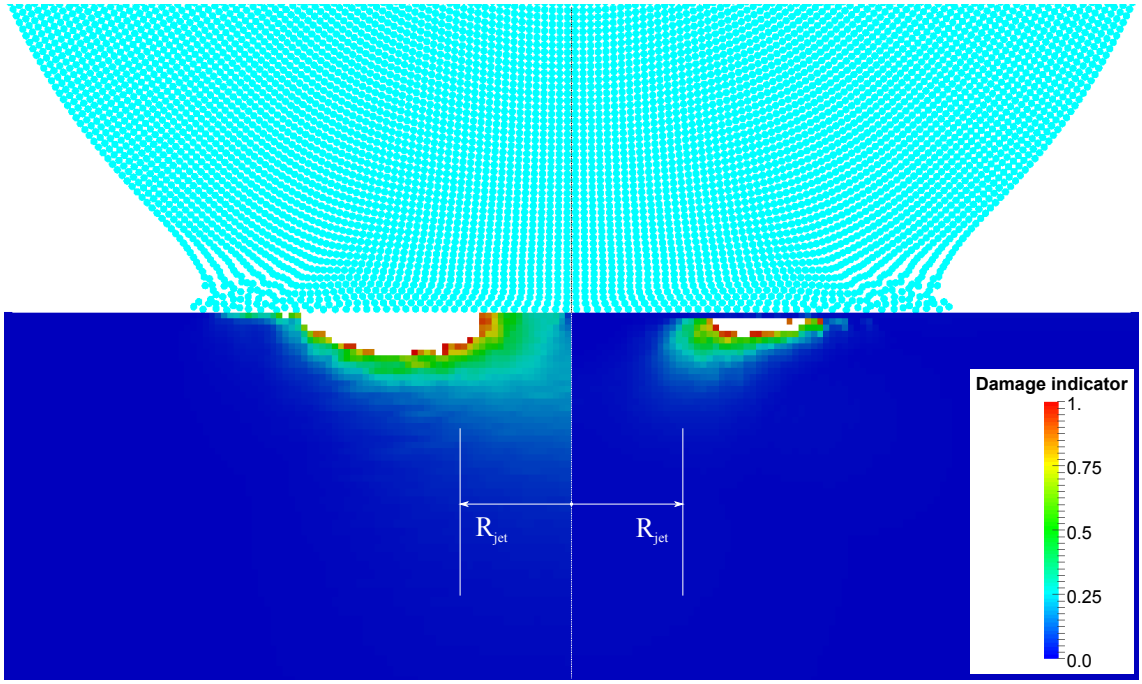

Figure 16: Damage indicator for $N_{\text{lim}} = 10$ Mcycles inside solid at $t = 460$ ns after impact according to general criterion E_g (left) and Dang Van criterion E_{DV} (right). Eroded elements are removed. Marks indicate the jetting location at $x = \pm R_{\text{jet}}$.